



## Electronic Delivery Cover Sheet

### **WARNING CONCERNING COPYRIGHT RESTRICTIONS**

The copyright law of the United States (Title 17, United States Code) governs the making of photocopies or other reproductions of copyrighted materials. Under certain conditions specified in the law, libraries and archives are authorized to furnish a photocopy or other reproduction. One of these specified conditions is that the photocopy or reproduction is not to be "used for any purpose other than private study, scholarship, or research". If a user makes a request for, or later uses, a photocopy or reproduction for purposes in excess of "fair use", that user may be liable for copyright infringement. This institution reserves the right to refuse to accept a copying order if, in its judgement, fulfillment of the order would involve violation of copyright law.



## Experimental observations of intersonic crack growth in asymmetrically loaded unidirectional composite plates

DEMIRKAN COKER† and ARES J. ROSAKIS‡

Graduate Aeronautical Laboratories, California Institute of Technology,  
Pasadena, California 91125, USA

[Received 26 November 1999 and accepted in revised form 25 May 2000]

### ABSTRACT

Some recent experimental observations of highly dynamic crack growth events in thick unidirectional composites are presented. The specimens used in this study were 48-ply thick unidirectional graphite–epoxy composite plates which were either symmetrically (mode I) or asymmetrically (mode II) loaded by impact in a one-point bend configuration with an edge pre-notch machined in the fibre direction. Moderate impact speeds of up to  $57 \text{ ms}^{-1}$  were used. The lateral shearing interferometric technique of coherent gradient sensing in conjunction with high-speed photography was used to visualize the failure process in real time. Mode-I cracks propagated subsonically with crack speeds increasing to the neighbourhood of the Rayleigh wave speed. For asymmetric mode-II types of loading the results revealed highly unstable and intersonic shear-dominated crack growth along the fibres. These cracks propagated with unprecedented speeds reaching  $7400 \text{ ms}^{-1}$ , a speed which is more than three times the shear wave speed of the composite and almost equal to the dilatational wave speed of the composite along the fibres. For intersonic crack growth, the interferograms featured a shock wave structure typical of disturbances travelling with speeds higher than one of the characteristic wave speeds in the solid. Evidence of large-scale frictional contact is also presented.

### §1. INTRODUCTION

Dynamic crack growth along weak planes is a predominant mode of failure in composites and other layered material systems. In the past few years, bimaterial fracture specimens, fabricated by bonding a stiff material to a compliant material (featuring a mismatch in wave speeds), have been used to demonstrate the importance of highly transient and dynamic crack growth in heterogeneous solids. It was observed that interfacial crack tip speeds rapidly approach and exceed the shear wave speed of the more compliant material (Lambros and Rosakis 1995a,b, Liu *et al.* 1995, Singh and Shukla 1996; Singh *et al.* 1997, Rosakis *et al.* 1998), thus reaching intersonic speeds with respect to this material. The term intersonic crack tip speed is defined here to denote the crack tip speed which lies between the shear wave speed and the longitudinal wave speed. For crack tip speeds above the shear wave speed a ray emanating from the crack tip across which there is a jump in shear tractions (shear shock wave) was predicted theoretically and was also observed experimentally

---

† Email: cokerd@aero.caltech.edu.

‡ Email: rosakis@aero.caltech.edu.

and numerically (Liu *et al.* 1995, Singh and Shukla 1996, Needleman and Rosakis 1999). These high crack tip speeds were obtained under loading conditions that promoted locally shear-dominated deformations at the crack tip which were further enhanced by the stress wave mismatch due to the mismatch of elastic properties across the interface. Also, the loading and the bond strength were such as to promote crack growth along the interface between the two solids (Lambros and Rosakis 1995a,b).

It has been observed that, in homogeneous materials in the absence of a preferable crack growth path, mode-II crack propagation is not likely because the crack naturally kinks and propagates in a direction that causes a local mode-I stress state around the crack tip. This is not necessarily true in solids that may be homogeneous with respect to their constitutive properties but may involve preferable crack paths in the form of weak planes of lower fracture toughness (inhomogeneous in terms of their fracture toughness). Unidirectional composites indeed fit this description if viewed from the 'macroscopic' point of view of a homogenized anisotropic theory. However, from the 'microscopic' viewpoint, unidirectional composite materials are locally inhomogeneous and are related to bimetals. Both material systems involve preferred crack growth directions and are also composed of a stiffer material (the fibre) bonded together with a more compliant material (the matrix). From a macroscopic point of view such solids can be viewed as homogeneous anisotropic as far as their elastic properties are concerned. However, they are still inhomogeneous regarding their fracture toughness properties. Indeed, from both the macroscopic and the microscopic viewpoints the common characteristic between unidirectional composites and bimetals is the existence of a weak straight line crack path which may accommodate growing cracks of both opening and shear modes. Because of the above observations and previous observations of intersonic crack growth in bimetals, unidirectional composites seem to be natural candidates for studying maximum permissible speeds of cracks of both modes in a system that is, at least macroscopically, homogeneous.

While purely elastodynamic crack growth theory excludes intersonic growth of mode-I cracks, it does not exclude the possibility of intersonic mode-II crack growth in isotropic or anisotropic homogeneous elastic solids in cases of self-similar cracks growing into their own planes (Broberg 1989). By forcing the shear cracks to grow along a straight line path, several researchers (Freund 1979, Georgiadis 1986, Broberg 1989, Huang *et al.* 1999) theoretically calculated the critical speed in isotropic materials at which intersonic crack growth is possible to be  $2^{1/2}c_s$ . For steady-state intersonic crack growth and in the absence of a cohesive crack tip structure this is the only speed at which the energy release rate is non zero and finite. Singular asymptotic analyses of intersonic crack growth in anisotropic materials were developed by Piva and Hasan (1996) and Huang *et al.* (1999). Shear cracks and dislocations moving intersonically in anisotropic solids were also discussed simultaneously by Gao *et al.* (1999). They predicted that, just as in isotropic materials, intersonic shear crack growth involving a finite energy release rate is possible at a specific critical speed  $v_c$ , which lies within the intersonic interval. However, in the case of anisotropic materials, this speed is the product of a complex function of the anisotropic material properties and the shear wave speed. More recently, Broberg (1999) developed a cohesive zone analysis to investigate the same phenomenon in orthotropic materials. The advantage of using a cohesive zone is that the pathology of predicting zero energy release rates through most of the intersonic regime is

eliminated. Broberg's work showed that the crack tip solution furnishes a finite and positive energy release rate throughout the intersonic regime, which has a distinct maximum at values close, but not equal, to the critical speed  $v_c$  predicted by the singular theories. Moreover, the proximity of that maximum to the critical speed  $v_c$  depends on the details of the cohesive model and coincides with  $v_c$  as the cohesive zone size shrinks to zero. Burrige *et al.* (1979), using a slip-weakening cohesive zone model concluded that, in isotropic materials, shear cracks propagating only at speeds between the critical speed  $2^{1/2}c_s$  and the longitudinal wave speed,  $c_l$  were stable in the intersonic regime.

To our knowledge, very few detailed experimental studies of either quasistatic or dynamic crack propagation in fibre-reinforced composites have been performed. Liu *et al.* (1998) investigated quasistatic fracture of polymer composites using the optical technique of coherent gradient sensing (CGS). Khanna and Shukla (1994) extended the theoretical model of Piva and Viola (1988) and used it to analyse measurements from strain gauges and to determine mode-I dynamic stress intensity factors for cracks propagating subsonically in unidirectional glass-epoxy composite laminates at constant speed. Lambros and Rosakis (1997), using CGS shearing interferometry in conjunction with high-speed photography, looked at the initiation and growth in thick unidirectional graphite-epoxy composite plates under symmetric one point impact loading. They observed crack tip speeds for mode-I loading which approached  $0.5c_R$ , where  $c_R$  is the speed of the Rayleigh surface waves travelling in the direction of the fibres of a half-space (one major direction of anisotropy). Finally, Liu *et al.* (1997) also used CGS and high-speed photography to investigate the dependence of the mode-I dynamic fracture toughness on the crack tip speed. In this study, the cracks were observed to propagate along the fibres as fast as  $0.8c_R$ .

The first experimental observations of intersonic crack tip speeds in unidirectional composite plates were made by Rosakis *et al.* (1997). Their experiments were subsequently numerically analysed by Haberman *et al.* (1997) and by Stout *et al.* (1998). Both experimental and numerical studies showed cracks growing at an average speed of  $5000 \text{ m s}^{-1}$  from the edges of a hole in a fibre-reinforced unidirectional composite plate after this plate was impacted in the direction of the fibres (figure 1). Two intersonic shear cracks propagating parallel to the fibres from the boundary of the hole towards the impact face can be observed in this figure. A distinctive shock wave structure emanating from the crack tip is also visible. These experiments, together with prior experience in bimetals, pointed to the possibility of intersonic crack growth under suitable shear dominated loading conditions and paved the way for the present detailed investigation of this phenomenon.

In this paper we present the first extensive experimental results pertaining to highly dynamic crack propagation in unidirectional graphite-epoxy composite plates under both mode-I and mode-II loading. The optical technique of CGS was used in conjunction with high-speed photography to scrutinize the crack growth process. Crack tip speed histories were then computed from the interferograms and the limiting crack tip speeds were thus determined. We show that intersonic crack growth takes place along the fibres in specimens loaded in such a way as to create predominately mode-II conditions at the crack tip. These intersonic shear cracks accelerate to very high speeds, both with respect to the maximum dilatational speed, which was very closely approached, and in absolute measure, up to  $7400 \text{ m s}^{-1}$ , which is the highest crack speed ever recorded. For cases in which the loading results in pure mode-I opening, only sub-Rayleigh crack growth is observed.

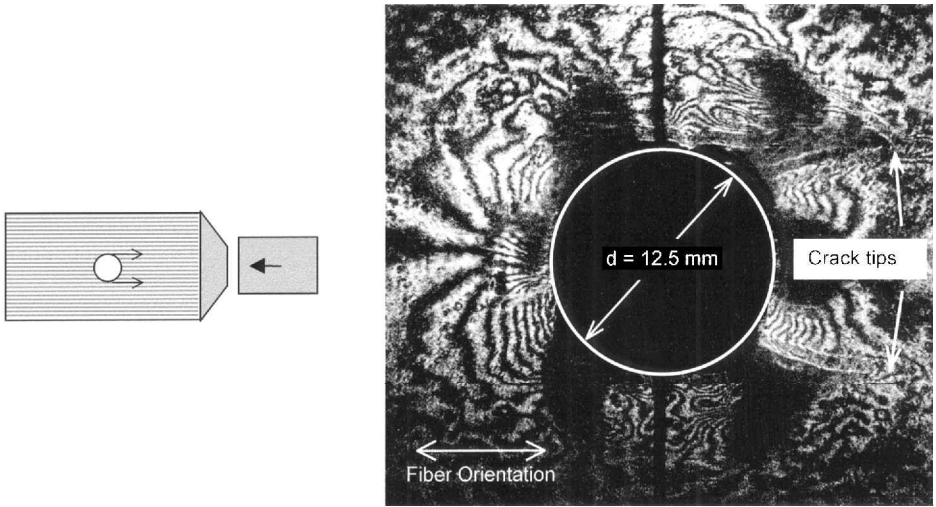


Figure 1. Cracks propagating at intersonic speeds after initiating from the edge of a hole in a unidirectional composite plate under impact loading along the fibres (Rosakis *et al.* 1997).

§2. MATERIAL AND SPECIMEN GEOMETRY

2.1. *Material and homogenized material properties*

A cross-section of the composite material is shown in figure 2. The fibre-reinforced unidirectional graphite–epoxy composite plates were manufactured by Composite Mirror Applications, Arizona, from 48 layers of graphite fibre and epoxy matrix pre-pregs laid up in the thickness direction to form a plate 6.3 mm thick. The fibre diameter was 7.3 μm and the volume fraction of the fibres in the pre-preg was 60–65%. The surface on one side of the composite plate was made optically flat by adding a thin layer of epoxy on one surface and then curing the composite specimen upon an optically flat glass plate. This surface was then made specularly reflective by coating with a thin layer of aluminium of 1–2 μm thickness in a vacuum deposition chamber. The glass transition temperature of epoxy matrix was 132°C (270°F). Poisson’s ratio for the matrix was 0.3 and for the fibre was 0.2.

The orientation of an orthonormal coordinate set with respect to the composite plate is shown in figure 2. The  $x_1$  axis is defined to lie along the fibres, the  $x_3$  axis is perpendicular to the plane of the composite surface (with an outward-pointing unit vector), while the  $x_2$  axis is perpendicular to the  $x_1$ – $x_3$  plane. If we assume that the fibres are randomly distributed in the epoxy matrix, then the  $x_2$ – $x_3$  plane can be taken as a plane of isotropy and, macroscopically, the material may then be considered a transversely isotropic material. The stresses are then related to the strains by the stiffness matrix as (Christensen 1979)

$$\begin{bmatrix} \sigma_1 = \sigma_{11} \\ \sigma_2 = \sigma_{22} \\ \sigma_3 = \sigma_{33} \\ \sigma_4 = \sigma_{23} \\ \sigma_5 = \sigma_{13} \\ \sigma_6 = \sigma_{12} \end{bmatrix} = \begin{bmatrix} c_{11} & c_{12} & c_{12} & 0 & 0 & 0 \\ c_{12} & c_{22} & c_{23} & 0 & 0 & 0 \\ c_{12} & c_{23} & c_{22} & 0 & 0 & 0 \\ 0 & 0 & 0 & c_{44} & 0 & 0 \\ 0 & 0 & 0 & 0 & c_{66} & 0 \\ 0 & 0 & 0 & 0 & 0 & c_{66} \end{bmatrix} \begin{bmatrix} \varepsilon_1 = \varepsilon_{11} \\ \varepsilon_2 = \varepsilon_{22} \\ \varepsilon_3 = \varepsilon_{33} \\ \varepsilon_4 = 2\varepsilon_{23} \\ \varepsilon_5 = 2\varepsilon_{13} \\ \varepsilon_6 = 2\varepsilon_{12} \end{bmatrix}, \tag{1}$$

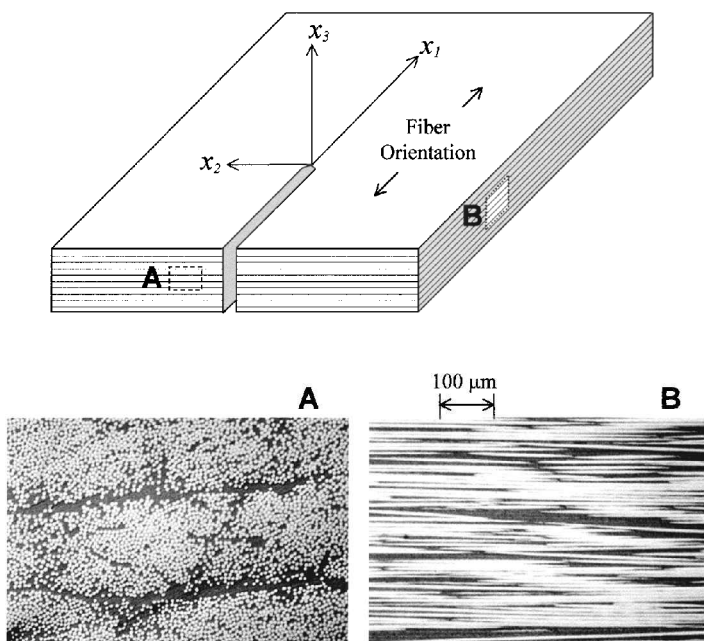


Figure 2. Cross-sectional view of fibre-reinforced unidirectional graphite-epoxy composite and definition of the coordinate axes with respect to the material symmetry axes.

where

$$c_{44} = \frac{c_{22} - c_{23}}{2}.$$

The stiffness matrix for a transversely isotropic matrix consists of five independent parameters:  $c_{11}$ ,  $c_{22}$ ,  $c_{12}$ ,  $c_{23}$ , and  $c_{66}$ . These parameters are related to the easily measurable mechanical moduli  $E_1$ ,  $E_2$ ,  $\nu_{23}$ ,  $\nu_{12}$  and  $\nu_{12}$ . These moduli can be expressed in terms of the original stiffness matrix components by

$$E_1 = c_{11} - \frac{2c_{12}^2}{c_{22} + c_{23}},$$

$$E_2 = \frac{(c_{22} - c_{23})(c_{11}c_{22} + c_{23}c_{11} - 2c_{12}^2)}{c_{11}c_{22} - c_{12}^2},$$
(2)

$$\nu_{12} = \frac{c_{12}}{c_{22} + c_{23}},$$

$$\nu_{21} = \frac{c_{12}(c_{22} - c_{23})}{c_{11}c_{22} - c_{12}^2} \text{ or } \frac{\nu_{12}}{E_1} = \frac{\nu_{21}}{E_2},$$

$$\nu_{23} = \frac{c_{23}c_{11} - c_{12}^2}{c_{11}c_{22} - c_{12}^2},$$
(3)

$$\mu_{12} = c_{66},$$

$$\mu_{23} = \frac{c_{22} - c_{23}}{2} = \frac{E_2}{2(1 + \nu_{23})}.$$

Table 1. In-plane material properties of the graphite–epoxy unidirectional composite.

|                                    |          |
|------------------------------------|----------|
| Three-dimensional stiffness matrix |          |
| $c_{11}$                           | 82.0 GPa |
| $c_{22}$                           | 11.1 GPa |
| $c_{12}$                           | 4.0 GPa  |
| $c_{23}$                           | 4.9 GPa  |
| $c_{66}$                           | 3.6 GPa  |
| $c_{44}$                           | 3.1 GPa  |
| Plane stress stiffness matrix      |          |
| $c'_{11}$                          | 80.5 GPa |
| $c'_{22}$                          | 9.0 GPa  |
| $c'_{12}$                          | 2.2 GPa  |
| $c'_{66} = c_{66}$                 | 3.6 GPa  |
| Elastic material properties        |          |
| $E_1$                              | 80 GPa   |
| $E_2 = E_3$                        | 8.9 GPa  |
| $\nu_{12} = \nu_{13}$              | 0.25     |
| $\nu_{23}$                         | 0.43     |
| $\mu^{12} = \mu^{13}$              | 3.6 GPa  |
| $\mu^{23}$                         | 3.1 GPa  |

The transversely isotropic elastic constants and the stiffness matrix for our graphite–epoxy unidirectional composite material are given in table 1. The reduced stiffness matrix for plane stress cases is also shown in table 1. This reduced stiffness matrix can be obtained from the mechanical properties through the following relations:

$$\begin{aligned}
 c'_{11} &= \frac{E_1}{1 - \nu_{12}\nu_{21}} = c_{11} - \frac{c_{12}^2}{c_{22}}, \\
 c'_{22} &= \frac{E_2}{1 - \nu_{12}\nu_{21}} = c_{22} - \frac{c_{23}^2}{c_{22}}, \\
 c'_{12} &= \frac{\nu_{21}E_1}{1 - \nu_{12}\nu_{21}} = c_{12} - \frac{c_{12}c_{23}}{c_{22}}, \\
 c'_{66} &= \mu_{12} = c_{66}.
 \end{aligned} \tag{4}$$

The shear modulus,  $\mu_{12}$ , was determined by quasistatic Iosipescu shear tests while uniaxial compression tests were conducted on an MTS hydraulic testing machine to determine Young's moduli,  $E_{11}$  and  $E_{22}$  and Poisson's ratio  $\nu_{12}$ . The calculated values for the stiffness components  $c_{11}$ ,  $c_{22}$  and  $c_{66}$  were also verified with those obtained from the plane strain longitudinal and shear wave speeds in the direction of the major axes through the following relations:

$$c_1^{\parallel} = \left( \frac{c_{11}}{\rho} \right)^{1/2}, \quad c_1^{\perp} = \left( \frac{c_{22}}{\rho} \right)^{1/2}, \quad c_s = \left( \frac{c_{66}}{\rho} \right)^{1/2}, \tag{5}$$

where  $c_1^{\parallel}$  denotes the dilatational wave speed parallel to the fibres while  $c_1^{\perp}$  denotes the dilatational wave speed perpendicular to the fibres, and  $c_s$  is the shear wave speed. The mass density  $\rho$  of the composite plate was  $1478 \text{ kg m}^{-3}$ . The longitudinal wave speeds perpendicular and parallel to the fibres and the shear wave speed were

Table 2. Characteristic plane-strain and plane-stress wave speeds.

|                                            | $c_I^{\parallel}$<br>( $\text{m s}^{-1}$ ) | $c_I^{\perp}$<br>( $\text{m s}^{-1}$ ) | $c_s$<br>( $\text{m s}^{-1}$ ) | $c_R^{\parallel}$<br>( $\text{m s}^{-1}$ ) |
|--------------------------------------------|--------------------------------------------|----------------------------------------|--------------------------------|--------------------------------------------|
| 5 MHz ultrasonic transducer (plane strain) | 7450 ± 100                                 | 2740 ± 100                             | 1560 ± 50                      | 1548                                       |
| Plane stress                               | 7380                                       | 2470                                   | 1560                           | 1548                                       |

obtained using ultrasonic pressure and shear transducers operating at a frequency of 5 MHz. These wave speeds are shown in table 2. It was noticed that significant deterioration in the material properties of the composite material took place within a 1 year period. The wave speed measurements carried out on virgin specimens a year before the experiments were conducted resulted in 30% higher wave speeds than the wave speeds obtained a year later. This change is attributed to humidity and temperature effects on the composite degrading the fibre–matrix interface during the time that the specimens were left sitting on the shelf. The wave speeds reported in table 2 are the values measured just before the fracture experiments were conducted. Also shown are the plane-stress longitudinal wave speeds obtained by replacing  $c_{ij}$  by the plane stress stiffness matrix  $c'_{ij}$  given in table 1. The bar wave speed in the graphite fibre was  $11\,230\text{ m s}^{-1}$  and the dilatational wave speed in epoxy was  $2500\text{ m s}^{-1}$ . The final row of table 2 shows the speed  $c_R^{\parallel}$  of Rayleigh waves propagating along the  $x_1$  direction (parallel to the fibres) on the surface of an anisotropic half-space and is obtained as the real root  $v = c_R^{\parallel}$  of the equation (Ting 1996)

$$\left( \frac{c'_{11}c'_{22} - c'^2_{12}}{c'_{22}c'_{66}} - \frac{\rho v^2}{c'_{66}} \right) \left[ \frac{c'_{22}}{c'_{11}} \left( 1 - \frac{\rho v^2}{c'_{66}} \right) \right]^{1/2} - \frac{\rho v^2}{c'_{66}} \left( 1 - \frac{\rho v^2}{c'_{11}} \right)^{1/2} = 0. \tag{6}$$

For the properties of our material,  $c_R^{\parallel} = 0.99c_s$ .

### 2.2. Specimen geometry

Two geometries of specimens were used in the experiments reported in this paper. The first geometry consisted of single-edge-notched (SEN) specimens of 127 mm width and 203 mm height (figure 3 (a)). The fibres were parallel to the shorter edge of the specimen. A notch of 25 mm in length and 1.5 mm in width was machined parallel to the fibres using a diamond saw. During the experiments, cracks initiated from this blunt notch. The blunted initial notch allows more strain energy to be stored prior to the generation of the dynamically growing crack and thus this bluntness controls (to a certain degree) the initiation crack tip speed. A sharp crack was used in one case in order to obtain a less abrupt start of crack propagation. As shown in the figure, these specimens were either loaded symmetrically or asymmetrically by impacting them with a steel projectile propelled by a gas gun. Very moderate impact speeds of up to  $57\text{ m s}^{-1}$  were used. The second type of specimen, used only for mode-II crack growth, was a 75 mm by 150 mm rectangular specimen with a 25 mm by 75 mm rectangular area removed from the centre of one edge as shown in figure 3 (b). After impact with a projectile, shear cracks initiated from the slightly rounded corners of the rectangular cut-out and propagated towards the impact area. This specimen configuration is an adaption of the circular hole geometry described by Rosakis *et al.* (1997).

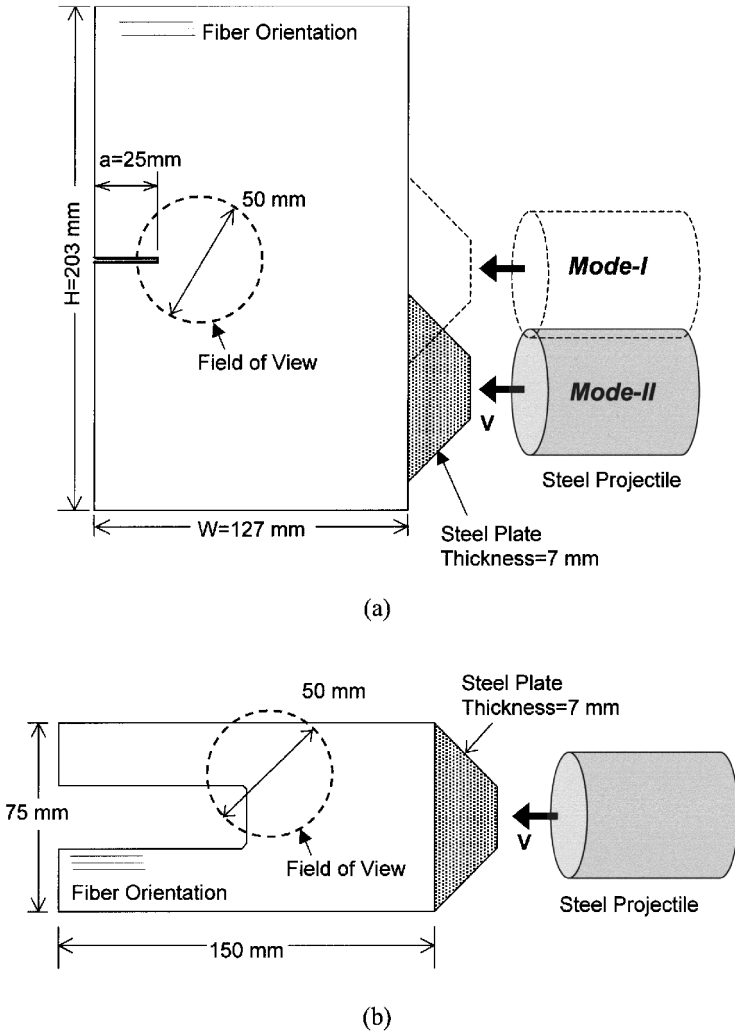


Figure 3. Geometry and dimensions for the composite specimens used in dynamic fracture experiments (thickness, 6.3 mm): (a) SEN geometry, (b) rectangular cut-out geometry for corner cracks.

### § 3. EXPERIMENTAL TECHNIQUE

A schematic diagram of the experimental set-up and of the optical technique of CGS is shown in figure 4. The specimen was subjected to impact loading through a projectile fired from a gas gun. The projectile was 75 mm long and 50 mm in diameter and was made of hardened steel. A steel piece was bonded to the specimen at the impact site to prevent crushing of the composite plate during impact and to induce a planar loading wave front. The projectile speed was varied between 20 and 30 m s<sup>-1</sup> for asymmetric loading and from 10 to 57 m s<sup>-1</sup> for symmetric loading.

The dynamic stress field produced by the impact loading wave leads to a time-varying out-of-plane displacement field on the surface of the composite plate. The optical technique of CGS by reflection was used in conjunction with high-speed

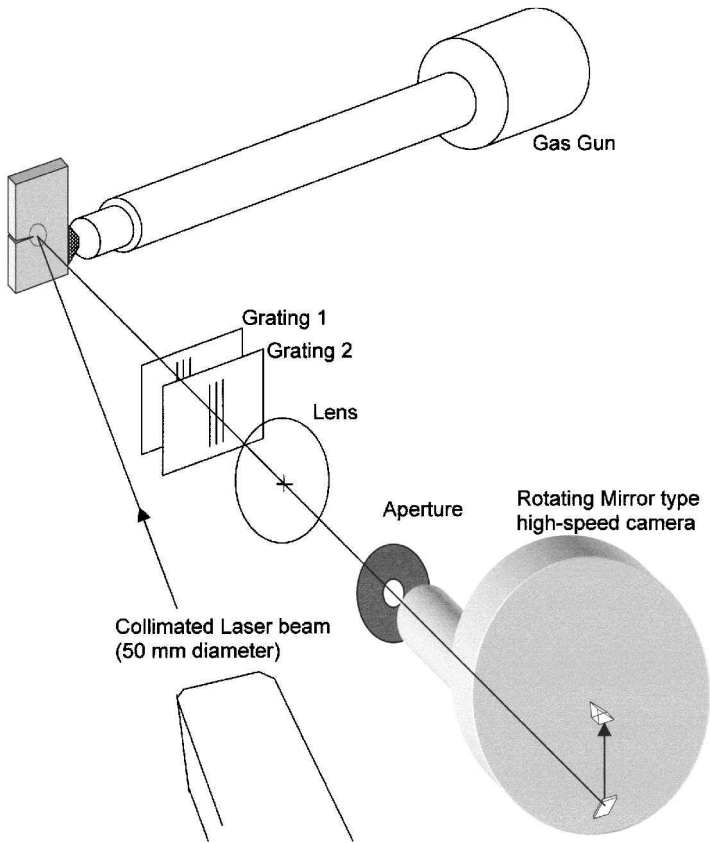


Figure 4. Schematic diagram of the experimental set-up and optical technique of CGS.

photography to record in real time the slopes of this out-of-plane deformation field. CGS is a full-field, lateral-shearing interferometer. The details of CGS can be found in several articles (Tippur *et al.* 1991, Rosakis 1993) and its application to crack initiation and subsonic growth in composite materials has been demonstrated before (Lambros and Rosakis 1997, Rosakis *et al.* 1997, Liu *et al.* 1998).

The experimental set-up used a coherent monochromatic collimated laser beam of 50 mm diameter which was incident on the specimen and was reflected from the initially optically flat and specularly reflective surface. Subsequently the reflected beam acquired an optical path difference due to the non-uniform specimen surface deformations generated near the crack tip after impact. The reflected beam passed through two high-density line diffraction gratings  $G_1$  and  $G_2$  of pitch  $p = 0.0254 \text{ mm}$  ( $40 \text{ lines mm}^{-1}$ ). The lines of the gratings were parallel to the  $x_2$  direction. The separation distance between these gratings is denoted by  $\Delta$  and is typically 40–60 mm. The gratings diffracted the reflected beam and recombined it with itself to form an interferogram. The light from the gratings was collected by a filtering lens  $L$  and a diffraction spot pattern was obtained on the filtering plane, which was located at the back focal plane of the lens  $L$ . By using a filtering aperture, all but either of the  $\pm 1$  diffraction orders were blocked. One of those two remaining diffraction spots was imaged to produce an interference pattern on the image plane of a camera.

CGS, when used in reflective mode, measures the in-plane gradients of out-of-plane displacements:

$$\frac{\partial u_3}{\partial x_1} = \frac{mp}{2\Delta}, \quad m = 0, \pm 1, \pm 2, \dots, \quad (7)$$

where  $u_3(x_1, x_2)$  is the out-of-plane displacement field of the reflective surface of the specimen,  $p$  and  $\Delta$  are the pitch and separation respectively of the two high-density gratings and  $m$  is the fringe order for the  $x_1$  gradient contours. According to the above equation, which holds when the lines of the gratings are parallel to the  $x_2$  direction, each CGS fringe is a locus of points that have the same slope in the  $x_1$  direction. Under conditions of plane stress,  $u_3(x_1, x_2)$  is related to the thickness averages of the stresses as follows (Lambros and Rosakis 1997 and Liu *et al.* 1998):

$$u_3 = \frac{h}{2}(b_{31}\sigma_{11} + b_{32}\sigma_{22}), \quad (8)$$

where  $h$  is the specimen thickness and  $b_{ij}$  are components of the compliance matrix  $\mathbf{b}$ , inverse to the stiffness matrix  $\mathbf{c}$  in equation (1), for the particular case of plane stress state.

The interference pattern was captured by a rotating mirror type high-speed camera (Cordin model 330A). The camera is capable of recording 80 frames at framing rates of up to  $2 \times 10^6$  frames  $s^{-1}$ . In the current experiments the interframe time in the experiments varied from 0.69–1.39  $\mu s$  and the image was recorded on 35 mm black-and-white film (Kodak TMAX-400). The laser used was an argon-ion laser operating at a wavelength of 514.5 nm in a pulsed mode of 8 ns pulse width. The recording process of the event commenced with the impact of the projectile on a strain gauge mounted on the steel plate, leading to a sharp voltage jump, thus triggering the pulsing of the laser.

## §4. EXPERIMENTAL OBSERVATIONS

### 4.1. Symmetric crack-tip loading

Symmetric mode-I crack tip deformations were attained by impacting the specimen symmetrically along the notch line by a steel projectile with projectile speeds varying from 10 to 57  $m s^{-1}$  (see figure 3(a)). A selected sequence of experimental CGS interferograms corresponding to mode-I crack initiation and propagation are shown in figure 5 for the highest impact speed of 57  $m s^{-1}$ . Only two out of the 80 interferograms are presented here. The two frames show the CGS interference fringe pattern that has developed around the notch tip 0.7  $\mu s$  before crack initiation and the fringe pattern corresponding to crack growth at 12.5  $\mu s$  after initiation. Using the entire sequence of pictures obtained from such an experiment the crack tip history is recorded as a function of time in figure 6(a) for mode-I symmetric loading. The crack length speed history is then obtained by differentiation by using a sectional quadratic three-point fit to the crack length history and is shown in figure 6(b). The crack is found to grow subsonically at 900  $m s^{-1}$  and accelerated to the Rayleigh wave speed  $c_R^{\parallel}$  of the composite in the direction of the fibres ( $c_R^{\parallel} = 1548 m s^{-1}$ ). If one regards the small oscillations in the calculated crack tip speeds as experimental error, the crack tip speed does not exceed the Rayleigh wave speed.

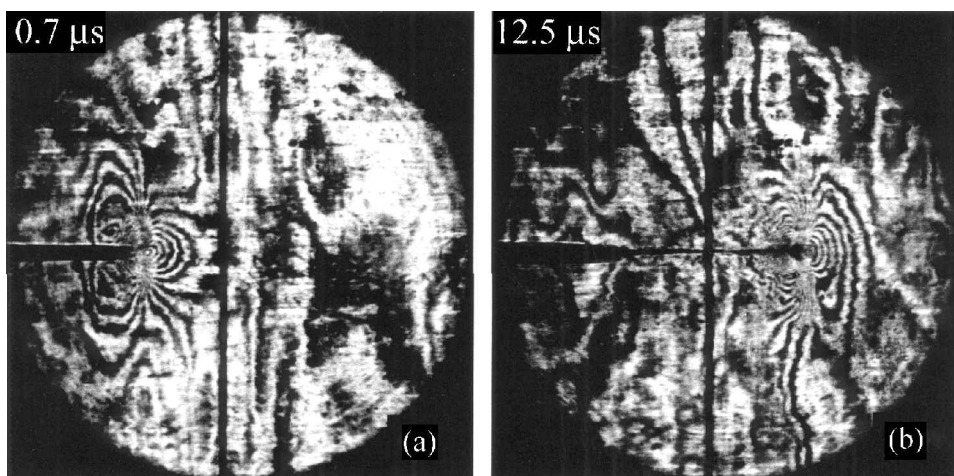


Figure 5. A sequence of CGS interferograms showing (a) mode-I crack tip loading and (b) crack propagation (mode I; SEN geometry; blunted crack; impact velocity,  $57 \text{ m s}^{-1}$ ). The field of view is a 50 mm circle around the notch tip.

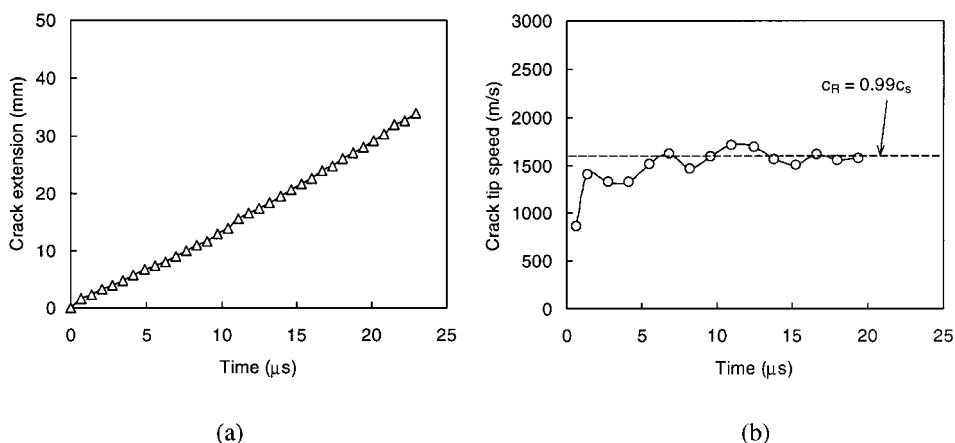


Figure 6. (a) Crack tip position and (b) crack tip speed histories for a crack propagating under symmetric mode-I loading. Same experiment as in figure 5.

#### 4.2. Shear dominated crack-tip loading

Asymmetric one-point bend impact experiments were conducted at a variety of impact speeds by impacting the specimen below the notch as shown in figure 3 (a). In these experiments the projectile speed varied from  $21$  to  $30 \text{ m s}^{-1}$ . For an impact speed of  $21 \text{ m s}^{-1}$  a sequence of four frames, selected from a sequence of 80 frames, taken with the high-speed camera at an interframe time of  $1.39 \mu\text{s}$  is shown in figure 7. The first three photographs show the CGS interference fringe patterns in an area of 50 mm diameter around the notch tip at various times before crack initiation. The last frame corresponds to a time of  $1.4 \mu\text{s}$  after crack initiation. The notch tip as well as the stress concentration surrounding it are both clearly visible in the first frame. The impact wave (compression) has propagated from one end of the plate to the

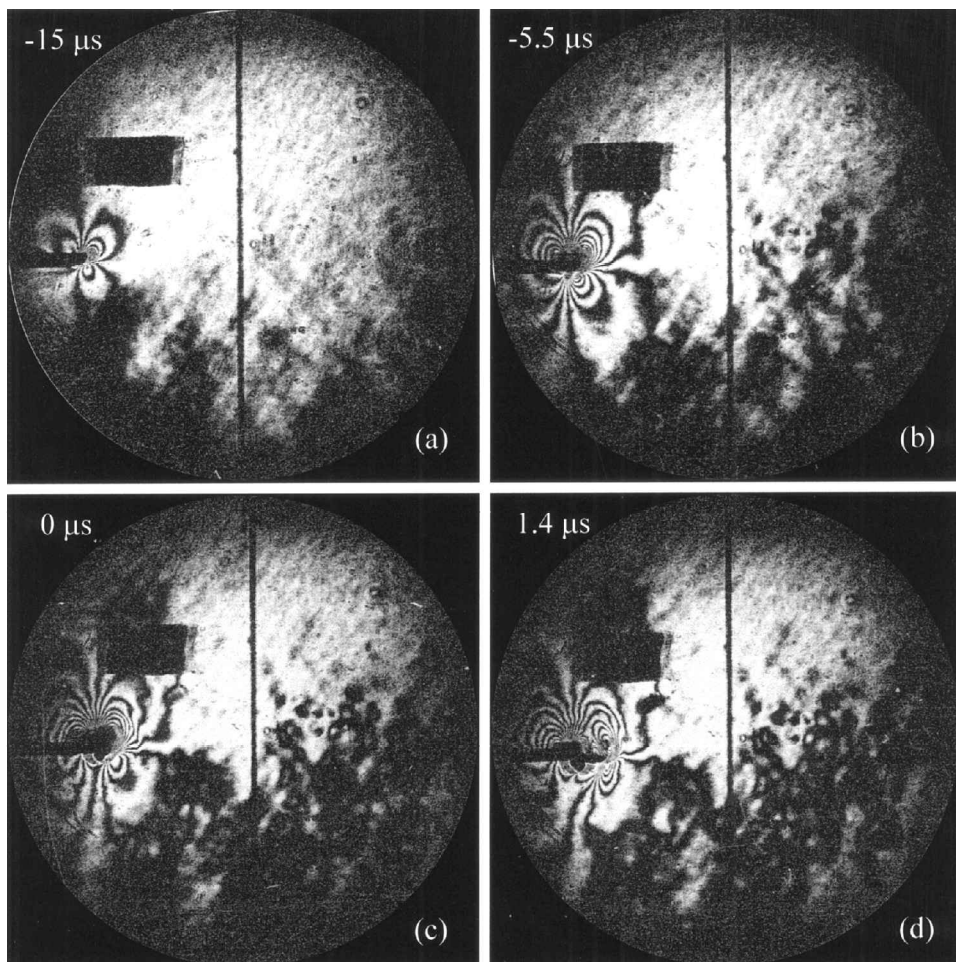


Figure 7. A sequence of CGS interferograms for shear-dominated crack tip loading, leading to crack initiation (mode II; SEN geometry; blunted crack; impact velocity,  $21 \text{ m s}^{-1}$ ). The field of view is a 50 mm circle around the notch tip.

other, has reflected as a tensile wave below the notch and has loaded the notch tip in a predominantly shear mode. A shadow of a marker for scaling appears at the top left-hand side. The vertical line in the centre is a streak line and is an artefact of the high-speed camera.

The notch tip stress concentration is seen to increase as the CGS fringes increase in size and number. The nature of the fringe pattern shows that the near tip conditions are primarily mode II. Indeed, they feature one fringe lobe in the back and two fringe lobes in the front, which is a distinctive characteristic of asymmetric mode-II CGS crack tip fringes (Rosakis 1993; Liu *et al.* 1998). These pictures show the fringe patterns around the notch tip just before (figure 7(c)) and just after crack initiation (figure 7(d)). However, in the last frame, a significant change takes place in which the fringe loops are squeezed backwards, indicating very high crack tip speeds and accelerations. Indeed, the average crack tip speed between these two frames is  $2100 \text{ m s}^{-1}$ , which is above the shear wave speed  $c_s = 1560 \text{ m s}^{-1}$ , for this material.

Also, the initial acceleration is of the order of  $10^9 \text{ m s}^{-2}$ . This dramatic change in shape is not observed in the mode-I crack growth experiments described above. The notch tip is loaded by the arrival of the loading wave initially at  $11 \mu\text{s}$  after impact and is fully loaded by the reflected wave at  $15 \mu\text{s}$ . The crack initiates from the notch tip at approximately  $32 \mu\text{s}$ .

A sequence of six CGS interferograms obtained at later times during the same experiment are shown in figure 8. These interferograms correspond to shear-dominated dynamic crack growth along the fibres. As the crack propagates, it accelerates and further dramatic changes can be observed in the shapes of the crack tip fringe patterns. The fringes are pushed further back and are elongated. The rear loop shape changes from rounded to a triangular wedge bounded by a line of highly concentrated fringes emerging from the crack tip at a well defined angle. This line is caused by a steep change in the stress gradients in a localized area, which later (as the crack exceeds the shear wave speed) forms a discontinuity in the stresses, that is a shear shock wave (for discussions of analytical and numerical models predicting such stress discontinuities during intersonic crack growth in bimetals and composites see Liu *et al.* (1995), Rosakis *et al.* (1998), Huang *et al.* (1999), and Needleman and Rosakis (1999)).<sup>†</sup> Finally, this line broadens into two parallel lines (a double shock wave) which intercept the crack surfaces over a finite area approximately 4–5 mm behind the crack tip. As will be discussed later, one possible reason for the observed double-shock-wave structure may be the existence of a finite size contact region behind the crack tip. A similar phenomenon of large-scale contact during intersonic crack growth in bimetals was initially reported in the experiments by Lambros and Rosakis (1995a,b) and numerically confirmed by Needleman and Rosakis (1999). In addition, the existence of a double-shock-wave structure resulting from contact in bimetals was discussed by Singh and Shukla (1996) and Rosakis, *et al.* (1998) and was analytically modelled by Huang *et al.* (1998). The slope of the shear shock wave changes as you move away from the crack tip, which may be due to unsteady crack growth. Furthermore, as the crack begins to move intersonically, the front fringe loops are pushed back by yet another line which is not as dramatic as the shock wave described above. Information regarding the crack tip deformation field cannot travel outside this outer line. The normal speed at which this outer line propagates is roughly  $2500 \text{ m s}^{-1}$ , which corresponds to the dilatational wave speed of epoxy, one of the two constituents of the composite plate. Thus, this second line of discontinuity seems to represent the dilatational shock wave in the additional epoxy layer on the surface due to a moving source (the crack tip) disturbance. The epoxy layer, which is added on the composite surface to make it optically flat, does not effect the homogenized composite properties. Although the speed of propagation of the outer line also seems to be consistent with  $c_1^\perp$ , a shock wave cannot form with

---

<sup>†</sup> In homogeneous isotropic materials the out-of-plane surface displacement field (and thus CGS) is sensitive to the sum of the normal stresses. For such solids, this sum does not suffer a jump and, as a result, CGS cannot be used to detect such discontinuities. In anisotropic solids, however, normal and shear deformations are coupled; the out-of-plane displacements are related to  $\sigma_{11}$  and  $\sigma_{22}$  directly and not only through their sum. As discussed by Huang *et al.* (1999), each of these stress components indeed suffers a jump, in the intersonic regime which now causes a jump in out-of-plane displacements and their gradients. It is this phenomenon which allows us to observe discontinuities in stresses indirectly in our experiments (for an expression relating the out-of-plane displacement and its gradients to the stress in orthotropic solids see Liu *et al.* (1998)).

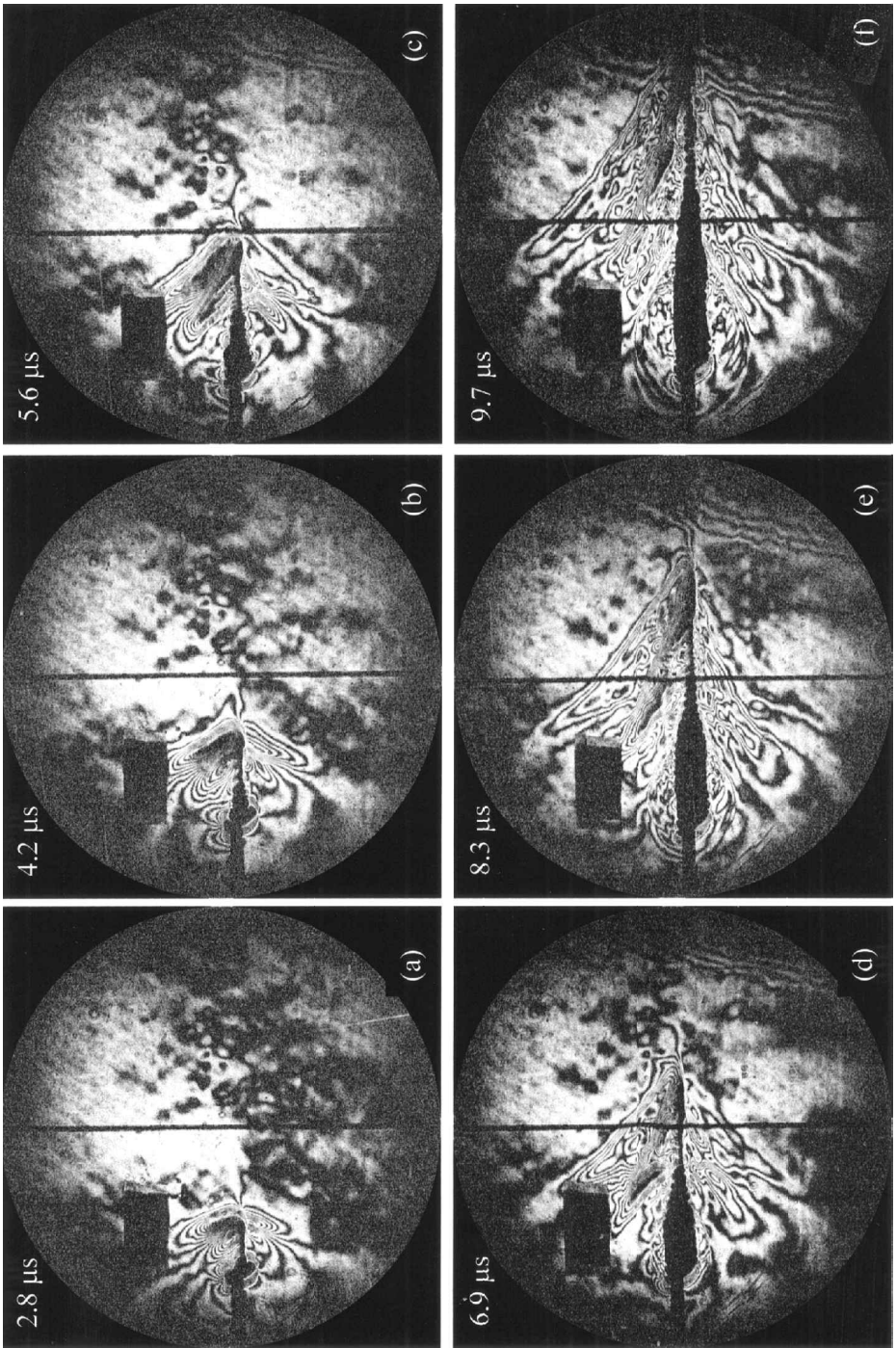


Figure 8. A selected sequence of CGS interferograms for an intersonically propagating crack tip. Same experiment as in figure 7.

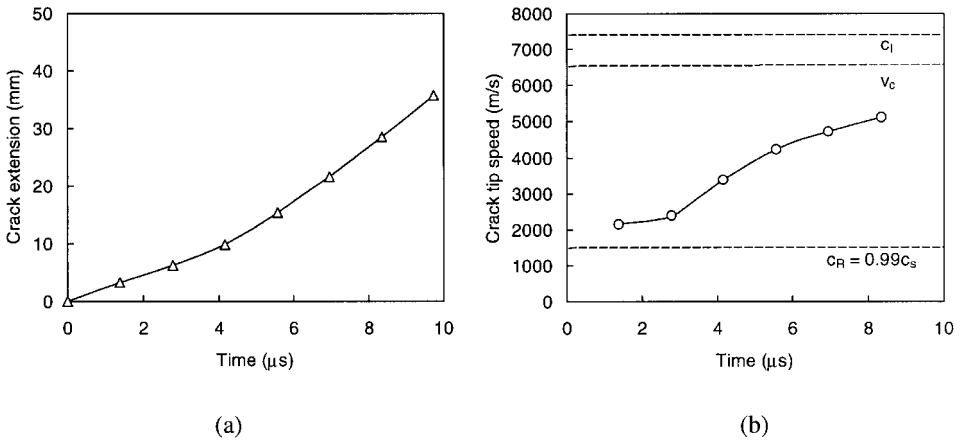


Figure 9. (a) Crack tip position and (b) crack tip speed histories for a shear-dominated crack propagating under asymmetric loading in a SEN specimen. Same experiment as in figure 7.

respect to  $c_1^\perp$  since the crack is moving intersonically parallel to the fibres. Thus, the existence of this line would not be predicted by models of intersonic crack growth based on homogenized theories of composites of the type performed by Huang *et al.* (1999).

The instantaneous location of the crack tip is known from each frame which together with the interframe time is used to determine the crack length history as well as the crack tip speed history. These are shown in figure 9(a) and (b) respectively. The crack tip speeds were calculated using a three-point polynomial fit to the crack tip length history. The crack tip speed approaches  $6000 \text{ m s}^{-1}$ , a speed which is 3.3 times higher than the shear wave speed and which is clearly intersonic. In this experiment the crack tip jumps immediately from rest to  $2100 \text{ m s}^{-1}$  becoming intersonic in the first frame after initiation and thus never crossing through the subsonic regime. Indeed, a subsonic crack tip speed was not observed at least within the time resolution of this experiment. The initial crack tip acceleration was also very high and was of the order of  $10^9 \text{ m s}^{-2}$ .

From figure 9(b) it can be seen that crack propagation had not reached steady state within our window of observation. A separate experiment was conducted under similar conditions with the field of view further downstream of the notch in order to investigate whether the crack tip speed eventually attains steady state conditions following the initial acceleration stage. In this experiment the impact velocity was  $28 \text{ m s}^{-1}$  and the interframe time was  $0.83 \mu\text{s}$ . A selected sequence of CGS fringe patterns is shown in figure 10. The crack tip position and speed history are plotted in figure 11(a) and (b) respectively. As already observed from the previous case, a shear shock wave and an outer dilatational shock wave, corresponding to the dilatational wave speed of the epoxy, are observed. However, in contrast with the previous experiment, a single dark line radiates from the crack tip. The first recorded crack tip speed is  $4000 \text{ m s}^{-1}$  as the crack appears within our field of view. The crack tip speed then increases and oscillates around an average speed of  $6500 \text{ m s}^{-1}$ . The maximum crack tip speed is  $7400 \text{ m s}^{-1}$  which is within experimental error, equal to the dilatational wave speed  $c_1$  along the  $x_1$  direction (parallel to the fibres). This is

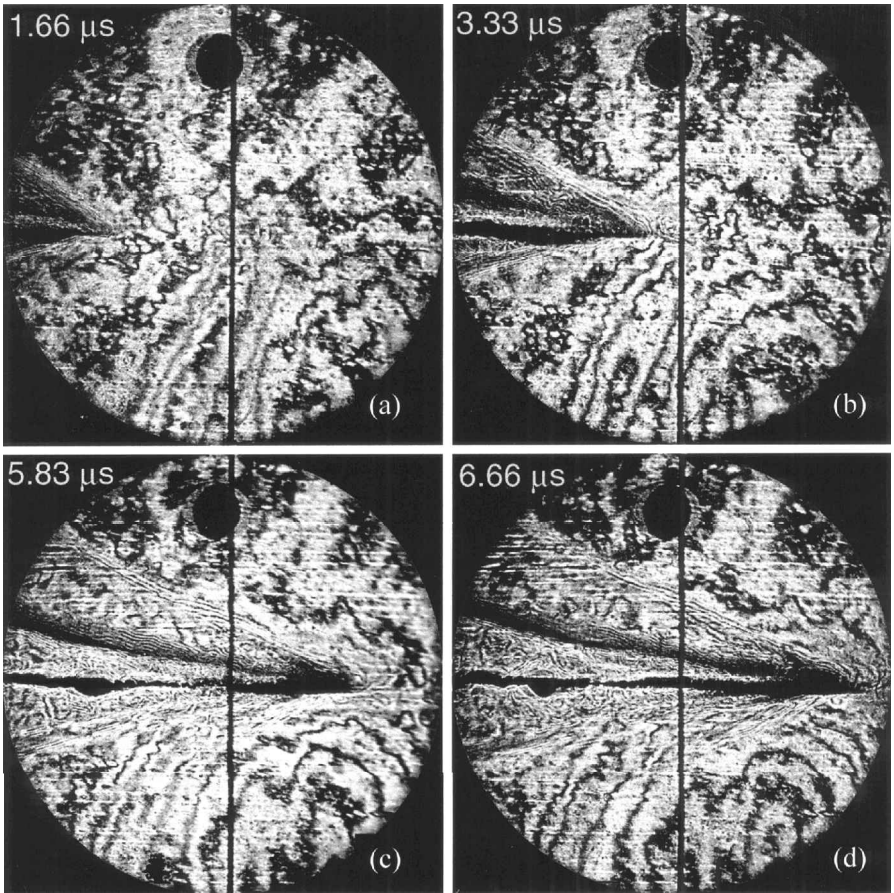
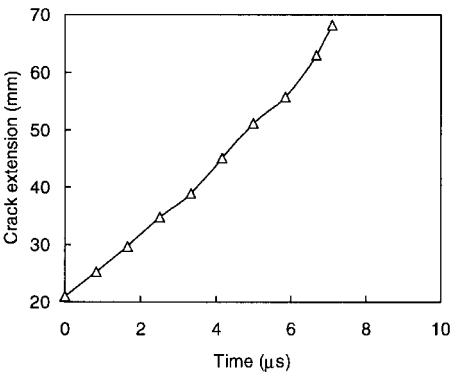
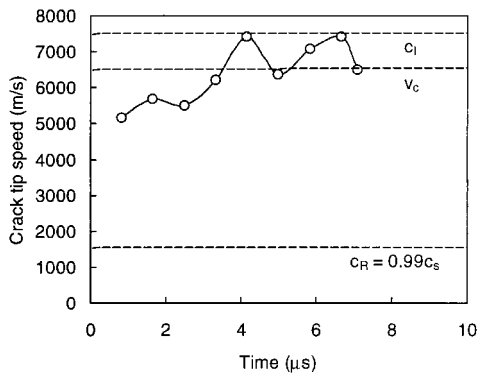


Figure 10. A selected sequence of CGS interferograms for an intersonically propagating crack tip (mode II; SEN geometry; blunted crack; impact velocity,  $28 \text{ m s}^{-1}$ ). The field of view is a 50 mm circle ahead of the notch tip.



(a)



(b)

Figure 11. (a) Crack tip position and (b) crack tip speed histories for a shear-dominated crack propagating under asymmetric loading in a SEN specimen. Same experiment as in figure 10.

the highest absolute crack tip speed ever observed in a laboratory setting or ever recorded in the open literature. However, it is inconclusive whether a strict steady state has been reached as the slope of the shock wave away from the crack tip is still varying.

In another experiment, a crack was initiated from an artificially sharpened initial notch, a condition imitating a pre-existing natural crack. A razor was used to extend the notch to a sharp crack and to promote initiation of crack growth at a lower level of far field shear stress. Indeed, the interferograms at crack initiation featured only a few fringes, indicating that crack initiation took place before there was significant stress concentration at the crack tip. Thus we were able to initiate mode-II crack growth at a low impact speed and driving force. A selected sequence of CGS interferograms are shown in figure 12. The crack length history and the calculated crack tip speed history are given in figures 13 (*a*) and (*b*) respectively. Since there was not enough energy stored before the crack initiated, the crack tip started subsonically at  $1100 \text{ m s}^{-1}$  and then entered the intersonic regime, levelling off at around  $6000 \text{ m s}^{-1}$ . Thus, when a sharp starter crack was used, the subsonic shear crack growth regime was found to be accessible and to occur at substantially lower impact speeds or far-field stress levels. Moreover, the subsonically moving shear crack was then able easily to enter the intersonic regime and eventually to reach speeds that are of the order of  $90\% c_1^{\parallel}$ . Indeed, as is clearly visible in figure 13, a fully developed double-shock structure is observed emanating from a 5 mm region behind the crack tip.

Yet another geometry that was tested was the plate with a rectangular cut-out in which we observed intersonic crack growth with a crack originating from the cut-out corner (figure 3 (*b*)). In this case the specimen is impacted by a steel projectile at  $21\text{--}28 \text{ m s}^{-1}$  and a plane wave propagates towards the cut-out. The wave reflects off the edge of the cut-out in the centre of the specimen whereas it continues to move along the two arms. This imposes a differential particle velocity to the centre beam which loads both corners of the cut-out in shear mode. A selected sequence of CGS interferograms are shown in figure 14. The loading phase of this experiment can be seen in the first frame. After initiation, the crack propagated to the right (towards the impact area) intersonically, featuring a characteristic shear shock wave structure similar to our previously described experiments. A typical crack tip speed history is shown in figure 15. The crack initiated within the intersonic interval at  $3000 \text{ m s}^{-1}$  and accelerated rapidly to just less than  $6000 \text{ m s}^{-1}$ .

## § 5. DISCUSSION

The general features of the CGS fringe patterns surrounding a shear-dominated crack propagating intersonically are summarized in figure 16. This figure shows a close-up area of 30 mm by 10 mm in size around the propagating crack. A distinct common feature that can be observed in all photographs shown in this figure is the existence of lines, or sets of lines, separating regions of various fringe densities. These lines radiate from the neighbourhood of the crack tip at different angles. The first (inner) set of lines bounds a relatively dark strip radiating from behind the crack tip at a shallow angle to the crack faces. These inner lines first appear as the crack begins to move intersonically. The dark strip between these lines could be a shadow spot (reflected light does not reach the film within the camera) or is the result of caustic formation (when the camera is not focused accurately on to the specimen surface). Both of these possibilities are due to intense gradients of the out-of-plane

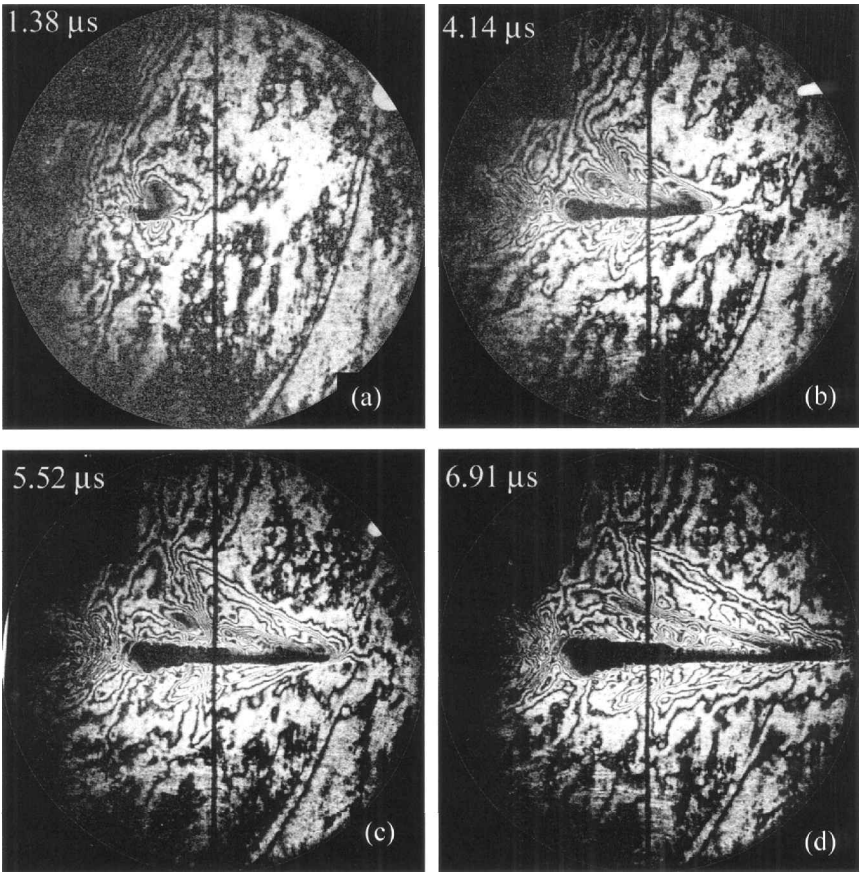


Figure 12. A selected sequence of CGS interferograms for an intersonically propagating crack tip for a crack initiating from a sharp pre-crack (mode II; SEN geometry; sharp crack; impact velocity,  $28 \text{ m s}^{-1}$ ). The field of view is around the initial crack tip.

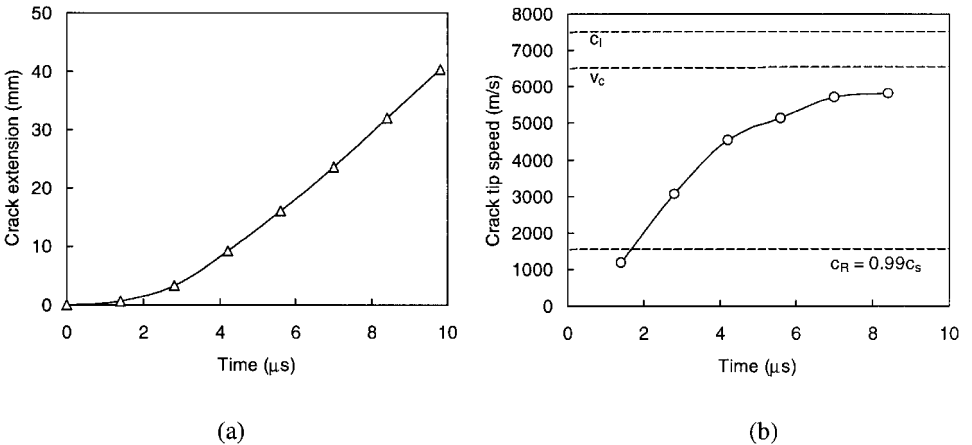


Figure 13. (a) Crack tip position and (b) crack tip speed histories for a shear-dominated crack propagating under asymmetric loading in a SEN specimen. Same experiment as in figure 12.

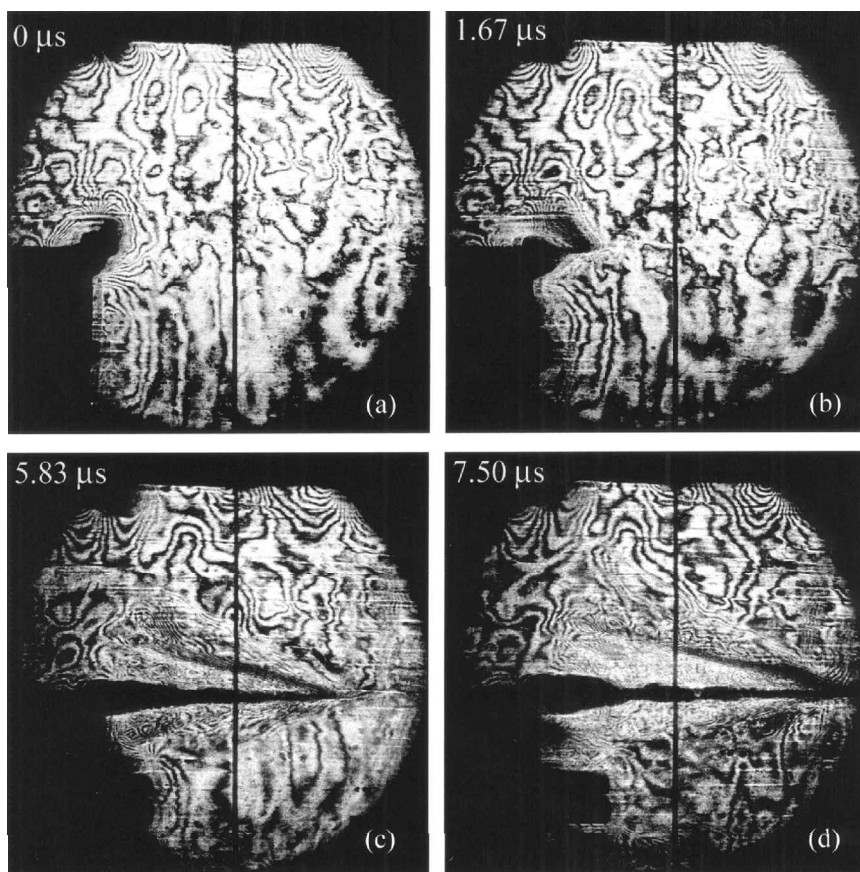


Figure 14. A selected sequence of CGS interferograms for an intersonically propagating crack tip that has initiated from a corner in a rectangular cut-out specimen (mode II; rectangular cut geometry; impact velocity;  $27 \text{ m s}^{-1}$ ).

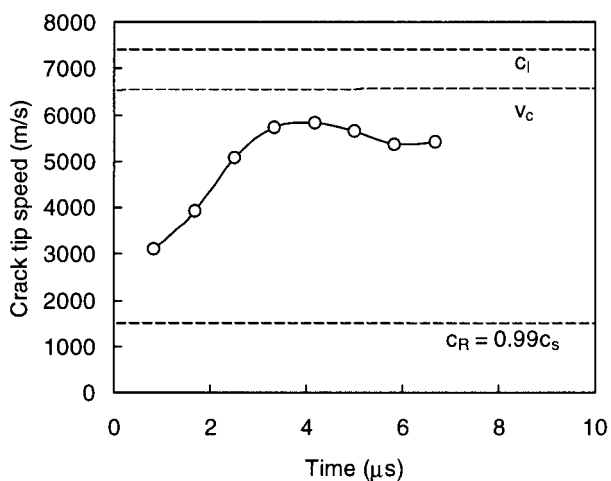


Figure 15. Crack tip speed history for a shear dominated crack propagating in a rectangular cut-out specimen. Same experiment as in figure 14.

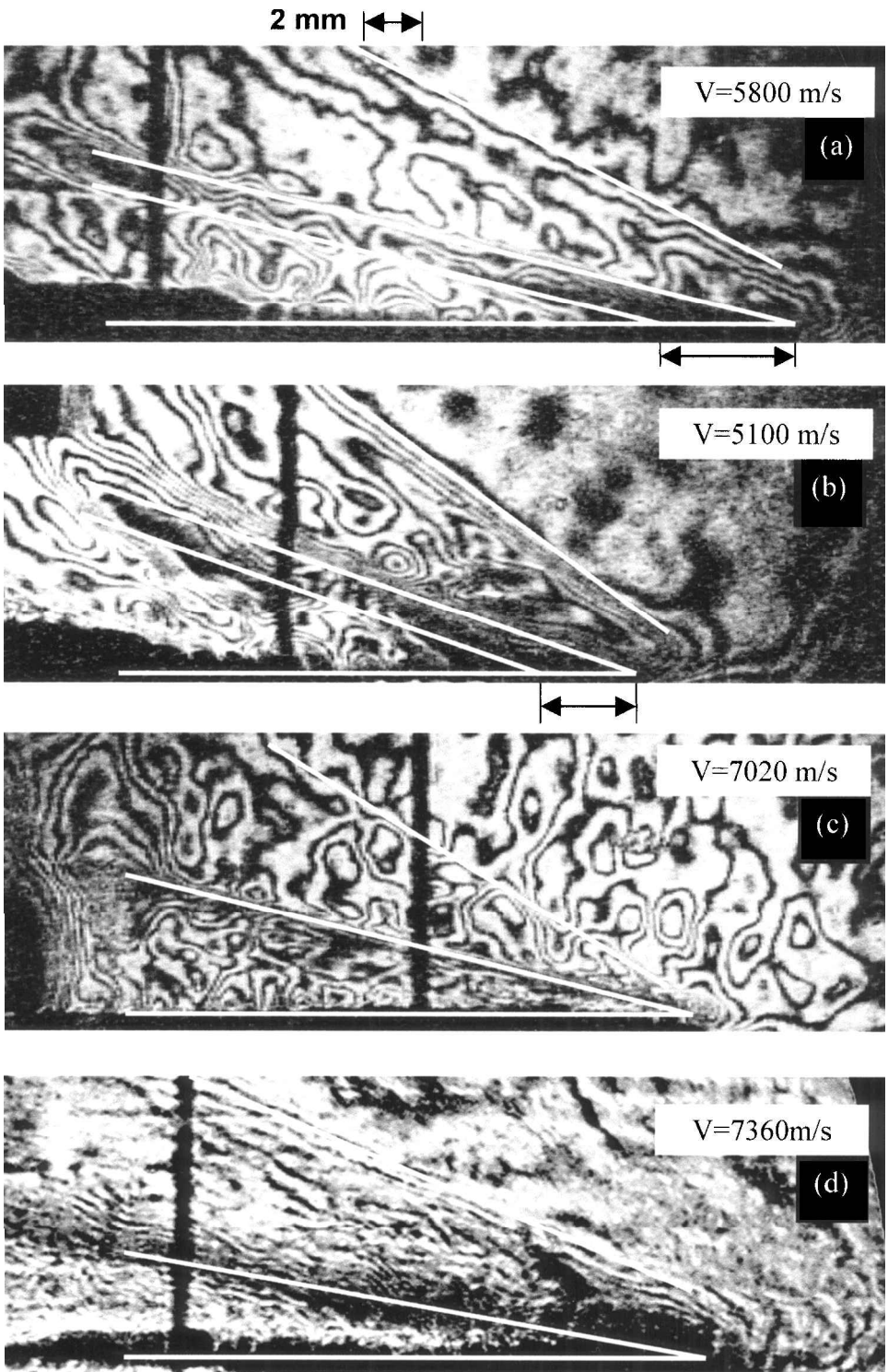


Figure 16. Close-up view of the crack tip in intersonically growing cracks at different speeds showing the shock wave structure.

displacements (Rosakis 1993). These lines arise when the crack tip speed is higher than the shear wave speed ( $c_s = 1560 \text{ m s}^{-1}$ ) and correspond to shear shock waves.

The second (outer) line radiates from the crack tip at a steeper angle to the crack faces. Indeed, as the crack begins to move intersonically, an outer envelope forms around the fringe pattern (bounded by this outer line) outside which information regarding the approaching crack tip has not been received. The normal speed at which this outer line propagates is roughly  $2500 \text{ m s}^{-1}$ , which corresponds to the dilatational wave speed of epoxy, one of the two constituents of the composite plate. Thus, this second line of discontinuity seems to represent the dilatational shock wave in the epoxy layer due to a moving source, that is the crack tip (note that the crack tip is purely supersonic compared with the dilatational wave speed of the epoxy matrix). The existence of this outer line cannot be predicted by theoretical derivations based on homogenized anisotropic models which are incapable of differentiating between the various individual phases of the composite.

A significant feature of the fringe patterns shown in figures 16(a) and (b) is the radiation of double lines or shear shock waves from behind the crack tip. The crack tip speeds of these two cases are  $5800$  and  $5100 \text{ m s}^{-1}$ , respectively. However, in figures 16(c) and (d) we can only see one distinct shear shock wave emanating from the crack tip at the higher speeds of  $7020$  and  $7360 \text{ m s}^{-1}$ , respectively. We suggest here that the existence of the double shock wave structure indicates the presence of a contact region behind the crack tip of the type that has been earlier observed during intersonic crack growth in bimetals (Lambros and Rosakis 1995a,b and Singh and Shukla 1996). At higher speeds the two distinct shock waves combine to give one shock wave radiating from the crack tip and the contact zone seems to vanish. This behaviour is reminiscent of the theoretical predictions of crack tip contact in bimetals (Liu *et al.* 1995). In this work, intersonic cracks were found to feature contact zones at the crack tip speeds below a characteristic speed ( $v \approx 2^{1/2}c_s$ ) which disappeared at higher speeds.

A view of the general trends in crack tip position history which are characteristic of many different experiments corresponding to very similar impact conditions can be observed in figure 17. This figure simultaneously displays results from many different experiments, shows the reproducibility of the observed experimental trends (within the same geometry and loading conditions) and allows us to obtain an average sense of the trends in the time history of crack tip position for both the mode-I and the mode-II cases. The corresponding crack tip speed histories plotted as a function of crack tip location are shown in figure 18. Mode-I cracks initiate at around  $900 \text{ m s}^{-1}$  and subsequently the crack speed increases to the neighbourhood of the Rayleigh wave speed. However, mode-II cracks initiate at around  $2000 \text{ m s}^{-1}$  (intersonic) and rapidly accelerate to above  $7000 \text{ m s}^{-1}$ . Eventually these cracks asymptotically approach a steady-state speed of approximately  $6500 \text{ m s}^{-1}$ .

In order to interpret the observed phenomena theoretical analyses were developed by Huang *et al.* (1999) and Gao *et al.* (1999). They obtained the asymptotic stress and displacement fields near a steady state, intersonically propagating crack tip in an orthotropic material. In this analysis, the composite was modelled as an elastic orthotropic homogeneous solid. For both the mode-I and the mode-II cases a prescribed straight line crack path was assumed. This models the experimental fact that both mode-I and mode-II cracks are confined to grow along the fibres of the unidirectional composite which correspond to the prescribed crack path of the analysis. The powers of the stress singularity for mode-I and mode-II cracks, denoted

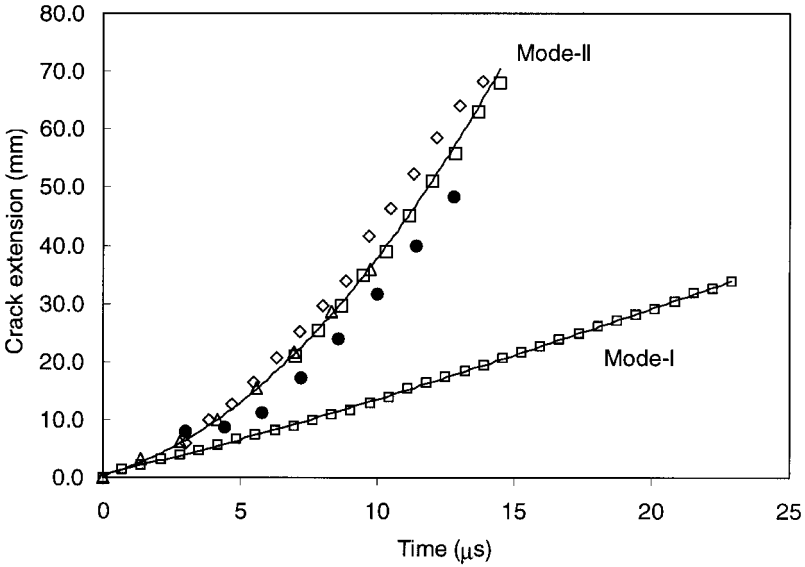


Figure 17. Crack tip position history for mode-I and mode-II cracks.

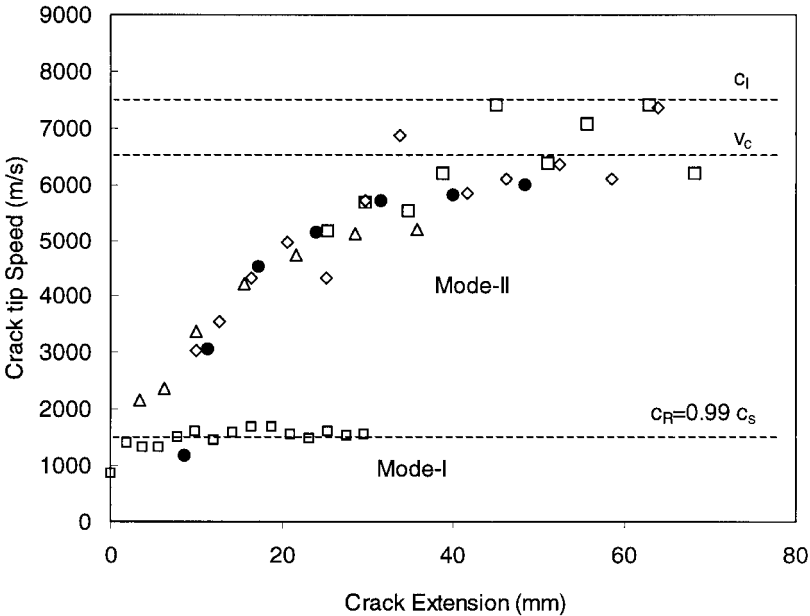


Figure 18. Crack tip speed as a function of crack tip position for mode-I and mode-II cracks.

here by  $q_I$  and  $q_{II}$  respectively, were found to vary with the material properties and crack tip speed. The power  $q_I$  of the stress singularity in mode I was found to be always larger than one half in the entire intersonic crack growth range, resulting in an unbounded energy release rate. In addition, close examination of the intersonic mode-I asymptotic field reveals that this unbounded energy release rate has a negative sign (negative infinity). This situation clearly indicates a physical impossibility

since a propagating crack tip needs a finite amount of positive energy to break the material bonds and cannot radiate out energy. Thus, it was concluded that within the assumptions of the singular crack tip model, a mode-I crack tip cannot propagate intersonically (for an equivalent argument for isotropic solids see Broberg (1989)). This conclusion is also supported by our experiments in which the crack tip speed never exceeded the shear wave speed within experimental error, regardless of how high the impact velocity of the projectile was (see figure 18). For mode II, intersonic crack growth the power  $q_{II}$  of the stress singularity, varies from zero to one half. It reaches one half only at a single critical crack tip speed  $v_c$ , where the energy release rate supplied by the elastic asymptotic field is finite and positive. Other intersonic crack tip speeds yielded a vanishing energy release rate. This critical crack tip speed, where  $q_{II} = \frac{1}{2}$ , is given by

$$\begin{aligned} v_c &= \left( \frac{c'_{11}c'_{22} - c'^2_{12}}{\rho(c'_{12} + c'_{22})} \right)^{1/2} \\ &= \left( \frac{E_1}{\rho(1 + \nu_{12})} \right)^{1/2} \\ &= \left( \frac{E_1}{\mu_{12}(1 + \nu_{12})} \right)^{1/2} c_s. \end{aligned} \tag{9}$$

Since a positive and finite energy supply is required to break the material bonds in front of the crack tip, this speed corresponds to the only possible *steady-state* intersonic crack growth speed according to the above asymptotic and singular steady state theory. Using the material properties given in table 1, this critical crack tip speed is approximately  $6600 \text{ m s}^{-1}$ . In our experiments the mode-II crack tips seem eventually to reach this value sometimes from below and sometimes from above. If there is not enough energy (e.g. at low impact speeds), then the crack tip asymptotically approaches this critical crack tip speed from below. If sufficient energy is imparted to the specimen, the crack tip unstably overshoots  $v_c$ . It eventually approaches this crack tip speed from above as the motion becomes increasingly steady.

The asymptotic analysis for mode II also predicts a shear shock wave emanating from the intersonically propagating crack tip. This would correspond to the ‘inner’ discontinuity line observed in the experiments to radiate from the crack tip at a shallow angle (see figures 16 (c) and (d)). The outer discontinuity line is not predicted since the theory does not account for the heterogeneous nature of the composite. The equation for the ray of singularity propagating with the crack tip is given by the expression  $\xi_1 + \mu_1 \xi_2 = 0$ , where  $\xi_1$  and  $\xi_2$  are the coordinate values with respect to a system of axes translating with the crack tip at an intersonic speed  $v$  and

$$\mu_1 = \left( \frac{(B^2 + 4AC)^{1/2} - B}{2A} \right)^{1/2}, \tag{10}$$

where

$$\begin{aligned} A &= c'_{22}c'_{66}, \\ B &= c'_{11}c'_{22} - (c'_{22} + c'_{66})\rho v^2 - c'^2_{12} - 2c'_{12}c'_{66}, \\ C &= (c'_{11} - \rho v^2)(\rho v^2 - c'_{66}). \end{aligned}$$

Using the material properties given in table 1 and a crack tip speed of  $7000 \text{ m s}^{-1}$ , the angle between the shear shock wave and the crack faces, calculated from this expression is  $18^\circ$  and that obtained from the experiments is  $15^\circ$ . The small discrepancy can be attributed to errors in the experimental determination of the crack tip speed, as well as to the possible variation in the material properties with strain rate, especially near the crack tip where the strain rates are expected to be very high.

## §6. CONCLUSIONS

Dynamic fracture experiments conducted in real time on pre-notched unidirectional fibre-reinforced graphite–epoxy plates indicate that mode-I (opening) cracks may only propagate subsonically along the fibres with respect to the homogenized anisotropic material properties with an upper bound of the Rayleigh wave speed. Mode-II (shear) cracks are, however, found to be capable of intersonic crack growth parallel to the fibres, typically accelerating from the vicinity of the shear wave speed to the dilatational wave speed  $c_{II}^{\parallel}$  along the fibre direction and eventually approaching a particular critical intersonic speed,  $v_c$ , determined by the homogenized anisotropic material properties. Under particular circumstances, a limited amount of unstable subsonic crack growth is also observed. Dual shock waves, which might imply a region of crack face contact, are formed at intersonic speeds lower than  $v_c$  while a single shock wave becomes visible at higher speeds. In absolute terms, unprecedented maximum crack tip speeds as high as  $7400 \text{ m s}^{-1}$  are observed.

## ACKNOWLEDGEMENTS

We acknowledge the support of the Office of Naval Research (Dr Y. D. S. Rajapakse, Scientific Officer) through grant N00014-95-0453 to California Institute of Technology and the support of the National Science Foundation through grant CMS9813100. Close interactions with Professor Y. Huang and Professor P. Geubelle of the University of Illinois, as well as with Professor H. Gao of Stanford University are also gratefully acknowledged.

## REFERENCES

- BROBERG, K. B., 1989, *Int. J. Fracture*, **39**, 1; 1999, *ibid.*, **99**, 1.  
 BURRIDGE, R., CONN, G., and FREUND, L. B., 1979, *J. geophys. Res.*, **85**, 706.  
 CHRISTENSEN, R. M., 1979, *Mechanics of Composite Materials* (New York: Wiley).  
 FREUND, L. B., 1979, *J. geophys. Res.*, **84**, 2199.  
 GAO, H., HUANG, Y., GUMBSCH, P., and ROSAKIS, A. J., 1999, *J. Mech. Phys. Solids*, **47**, 1941.  
 GEORGIADIS, H. G., 1986, *Int. J. Fracture*, **30**, 175.  
 HABERMAN, K. S., BENNET, J. G., LIU, C., STOUT, M. G., and ROSAKIS, A. J., 1997, Technical Report LA-13272-MS, Los Alamos, New Mexico.  
 HUANG, Y., WANG, W., LIU, C., and ROSAKIS, A. J., 1998, *J. Mech. Phys. Solids*, **46**, 2233; 1999, *ibid.*, **47**, 1893.  
 KHANNA, S. K., and SHUKLA, A., 1994, *Engng Fracture Mech.*, **47**, 345.  
 LAMBROS, J., and ROSAKIS, A. J., 1995a, *J. Mech. Phys. Solids*, **43**, 169; 1995b, *Proc. Roy. Soc. A*, **451**, 711; 1997, *Comput. Sci. Technol.*, **57**, 55.  
 LIU, C., HUANG, Y., and ROSAKIS, A. J., 1995, *J. Mech. Phys. Solids*, **43**, 189.  
 LIU, C., ROSAKIS, A. J., ELLIS, R. W., and STOUT, M. G., 1997, GALCIT SM Report 97-10, California Institute of Technology, Pasadena, California; 1998, *Int. J. Fracture*, **90**, 355.  
 NEEDLEMAN, A., and ROSAKIS, A. J., 1999, *J. Mech. Phys. Solids*, **47**, 2411.  
 PIVA, A., and HASAN, W., 1996, *J. appl. Mech.*, **63**, 933.  
 PIVA, A., and VIOLA, E., 1988, *Engng. Fracture Mech.*, **29**, 535.

- ROSAKIS, A. J., 1993, *Experimental Techniques in Fracture*, edited by J. S. Epstein (New York: VCH), pp. 327–425.
- ROSAKIS, A. J., LIU, C., STOUT, M. G., and COKER, D., 1997, GALCIT SM Report 97-8, California Institute of Technology, Pasadena, California.
- ROSAKIS, A. J., SAMUDRALA, O., SINGH, R. P., and SHUKLA, A., 1998, *J. Mech. Phys. Solids*, **46**, 1789.
- SINGH, R. P., J. LAMBROS, SHUKLA, A., and ROSAKIS, A. J., 1997, *Proc. R. Soc. A*, **453**, 2649.
- SINGH, R. P., and SHUKLA, A., 1996, *J. appl. Mech.*, **63**, 919.
- STOUT, M. G., LIU, C., ELLIS, R. W., HABERMAN, K. S., BENNETT, J. G., WILLIAMS, P. O., ADESSIO, F. L., and ROSAKIS, A. J., 1998, *Advances in Design Testing and Analysis, Proceedings of the 11th International Conference on Experimental Mechanics*, Oxford, 24–28 August, 1998, edited by I. M. Allison (Rotterdam: Balkema–Brookfield), pp. 187–192.
- TING, T. C. T., 1996, *Anisotropic Elasticity, Theory and Applications* (Oxford University Press).
- TIPPUR, H. V., KRISHNASWAMY, S., and ROSAKIS, A. J., 1991, *Int. J. Fracture*, **48**, 193.